local primordial non-Gaussianity from the large-scale clustering of photometric DESI luminous red galaxies

Mehdi Rezaie[1,2], Ashley J. Ross[3], Hee-Jong Seo[2], Hui Kong[3], Edmond Chaussidon[4], Anna Porredon[3], Lado Samushia[1], Rongpu Zhou[5], Alex Krolewski[6,7,8], Arnaud de Mattia[4], Jose Bermejo[?], Florian Beutler[9], Christophe Yeche[4], Nathalie Palanque-Delabrouille[4,5], Klaus Honscheid[3,10], and DESI Builders

[1]*Department of Physics, Kansas State University, 116 Cardwell Hall, Manhattan, KS 66506, USA*
[2]*Department of Physics and Astronomy, Ohio University, Athens, OH 45701, USA*
[3]*Center for Cosmology and AstroParticle Physics, The Ohio State University, 191 West Woodruff Avenue, Columbus, OH 43210, USA*
[4]*IRFU, CEA, Universite Paris-Saclay, F-91191 Gif-sur-Yvette, France*
[5]*Lawrence Berkeley National Laboratory, 1 Cyclotron Road, Berkeley, CA 94720, USA*
[6]*Department of Physics and Astronomy, University of Waterloo, 200 University Ave W, Waterloo, ON N2L 3G1, Canada*
[7]*Perimeter Institute for Theoretical Physics, 31 Caroline St. North, Waterloo, ON N2L 2Y5, Canada*
[8]*Waterloo Centre for Astrophysics, University of Waterloo, 200 University Ave W, Waterloo, ON N2L 3G1, Canada*
[9]*Institute for Astronomy, University of Edinburgh, Royal Observatory, Blackford Hill, Edinburgh EH9 3HJ, UK*
[10]*Department of Physics, The Ohio State University, 191 West Woodruff Avenue, Columbus, OH 43210, USA*

ABSTRACT
This paper uses the large-scale clustering of luminous red galaxies selected from the Dark Energy Spectroscopic Instrument Legacy Imaging Surveys Data Release 9 to constrain the local primordial non-Gaussianity (PNG) parameter $f_{\rm NL}$. Using the angular power spectrum, we thoroughly investigate the impact of various photometric systematic effects, such as those caused by Galactic extinction and varying survey depth. Simulations are utilized to construct covariance matrices, evaluate the robustness of our pipeline, and perform statistical tests to assess whether spurious fluctuations are properly mitigated and calibrated. Using modes from $\ell = 2$ to 300, we find $X1 < f_{\rm NL} < X2$ with our conservative and $X1 < f_{\rm NL} < X2$ with extreme treatment of imaging systematics, both at 68% confidence. While our results are consistent with zero PNG, but we show that the understanding of imaging systematics is of paramount importance to obtain unbiased constraints on $f_{\rm NL}$.

Key words: cosmology: inflation - large-scale structure of the Universe

1 INTRODUCTION

Current observations of the cosmic microwave background (CMB), large-scale structure (LSS), and supernovae (SN) are explained by a cosmological model that consists of dark energy, dark matter, and ordinary luminous matter, which has gone through a phase of rapid expansion, known as *inflation*, at its early stages (see, e.g., Weinberg et al. 2013). The theory of inflation elegantly addresses fundamental issues with the hot Big Bang theory, such as the isotropy of the CMB temperature, absence of magnetic monopole, and flatness of the Universe (see, e.g., Ryden 2002). At the end of inflation, the Universe was reheated and primordial fluctuations are generated to seed the subsequent growth of structure (Kofman et al 1994, Bassett et al 2006, Lyth and Liddle 2009). While the presence of an inflationary era is certain but the details of the inflation field still remain

highly unknown, and statistical properties of primordial fluctuations pose as one of the puzzling questions in modern observational cosmology. Analyses of cosmological data have revealed that initial conditions of the Universe are consistent with Gaussian fluctuations (Guth and Kaiser 2005); however, there are some classes of models that predict some levels of non-Gaussianities in the primordial gravitational field. In its simplest form, primordial non-Gaussianity depends on the local value of the gravitational potential ϕ and is parameterized by a nonlinear parameter $f_{\rm NL}$ (Komatsu & Spergel 2001),

$$\Phi = \phi + f_{\rm NL}[\phi^2 - <\phi^2>]. \tag{1}$$

Standard slow roll inflation predicts $f_{\rm NL}$ to be of order 10^{-2}, while multifield theories predict considerably higher values than unity (see, e.g., Putter et al 2017). Therefore, a robust measurement of

f_{NL} can be considered as the first stepping stone toward better understanding the physics of the early Universe. PNG alters local number density of galaxies by coupling the long and small wavelength modes of dark matter gravitational field, and as a result it introduces a scale-dependent shift in halo bias (see, e.g., Dalal et al. 2008; Slosar et al. 2008),

$$\Delta b \sim f_{NL} \frac{(b-p)}{k^2}, \qquad (2)$$

where p determines the response of the tracer to the halo gravitational field. Assuming universality of the halo function, i.e., the occupation of halos can be determined from the mass, $p = 1$. However, numerical simulations have shown the halo mass function of tracers that are result of recent mergers could depend on more parameters other than mass, and thus $p = 1.6$. Because of the k^{-2} dependence, the effect of local primordial non-Gaussianity leaves its signature on the large scales in the two-point clustering of large-scale structure.

Current tightest bound on f_{NL} comes from the three-point clustering analysis of the CMB temperature anisotropies by the Planck satellite, $f_{NL} = 0.9 \pm 5.0$ (Akrami et al. 2019). Next generations of CMB experiments, will improve this constraint but since CMB is limited by cosmic variance, it alone cannot further enhance to break the degeneracy amongst inflationary models (see, e.g., Ade et al 2019). However, combining CMB with LSS data could cancel cosmic variance, partially if not completely, and enhance these limits to a precision level required to differentiate between various inflationary models (see, e.g., Schmittfull & Seljak 2018). Constraining f_{NL} with the three point clustering of LSS is also hindered by the late-time nonlinear effects raised due to structure growth (see, e.g., Baldauf et al 2011), and this leaves the scale-dependent bias effect a smoking gun for constraining local PNG with LSS.

Measuring f_{NL} using the scale-dependent bias is however very challenging due to the presence of systematic effects which cause excess clustering signal on the same scales sensitive to f_{NL}. These systematics can be broadly classified into theoretical and observational. Major theoretical systematic effects are caused by the geometry of survey – a fact that we never observe the full night sky – which results in coupling different angular modes (see, e.g., Beutler et al. 2014, de Mattia and Ruhlmann-Kleider 2019). The other effect is commonly referred to as integral constraint and is raised due to our estimation of the mean density directly from data itself, which pushes the clustering signal on modes near the size of survey to zero (Peacock and Nicholson 1991, Wilson et al 2015). Ignoring any of these effects leads to biased f_{NL} constraints (see, e.g., Riquelme et al 2022). On the other hand, observational systematics are primarily caused by varying imaging properties across the sky or calibration issues which leave spurious fluctuations in target density field (see, e.g., Huterer et al 2013). This type of systematic error is much more difficult to handle and has hindered previous studies of local PNG with galaxy and quasar clustering (see, e.g., Ho et al. 2015). For instance, Pullen & Hirata (2013) found that the level of systematic contamination in the quasar sample of SDSS DRX does not allow a robust f_{NL} measurement. These imaging systematic issues are expected to be severe for wide-area galaxy surveys that observe the night sky closer to the Galactic plane and attempt to loosen the selection criteria to incorporate fainter targets. Beside canceling cosmic variance, cross correlating different tracers is a technique to alleviate systematic error, as each tracer might respond differently to a source of systematics. Giannantonio et al 2014 presents constraints using the integrated Sachs Wolfe effect. McCarthy et al (2022) uses cosmic infrared background as a proxy for halos and cosmic microwave background lensing as a proxy for matter, finding no evidence for local primordial non-Gaussianity.

DESI utilizes robots to collect 5000 spectra simultanously, and it is going to deliver an unparalleled amount of spectroscopic data up to redshift X, which will complete our understanding of the energy contents of the Universe. With the volume probed and assuming imaging systematics are under control, DESI along with other upcoming surveys such as Rubin Observatory, and SphereX are forecast to yield unprecedented constraints on f_{NL} as well (Abell et al 2009, Dore et al 2014, Aghamousa et al 2016). DESI preselects its targets from its dedicated imaging surveys, as known as Legacy Surveys, which are collected between 2014 and 2019 from three ground-based telescopes in Chile and the US. Understanding and calibration of systematic error in DESI imaging data is of paramount importance since these effects from imaging catalogs could potentially be inherited into spectroscopic catalogs, and thus impact the science one can do with DESI data. DESI targets galaxies and quasars and the effect of observational systematics in the DESI imaging data have been studied in great detail in Kitanidis et al (???), Rezaie et al (2021), Zhou et al (2021), and Chaussidon et al (2022). Improving methods to characterize systematic error in these samples is also important for measuring f_{NL}. We have a lot of amazing methods to eliminate the effect of imaging systematics. Some of these methods are based on cross correlating the map of target density with maps for imaging properties, while the other methods use a regression analysis to regress out the modes of imaging properties from the target density. While these methods are essentially the same, but they have their own limitations and constraints. For instance the cross correlation techniques can only be used for 2D data and could be time consuming for a large survey, but the template-based regression methods could be fast but yield biased results or remove some of the true clustering signal. Specifically related to the regression based methods, there is a little effort to calibrate and characterize the amount of the true clustering signal which is removed during the cleaning process. For studies like BAO and RSD, these effect might not matter (see, e.g., Merz et al 2021), however, as these effects are very prominent on large scales (see, e.g., Rezaie et al 2020, Mueller et al 2022), they could introduce biases in f_{NL} constraints.

With the high importance of systematic error, the primary focus of this paper is to present an exquisite study of imaging systematic error and characterization of mitigation biases for measuring f_{NL}. We also present enhanced statistical tools to address the data quality and significance of residual systematic error. In this paper, we use the photometric sample of luminous red galaxies from the DESI Legacy Imaging Surveys Data Release 9, hereafter referred to as DR9, to constrain the local primordial non-Gaussianity parameter f_{NL}, while testing the robustness of our results against various sources of systematic effects. We also make use of spectroscopic data from DESI Survey Validation to determine the redshift distribution of galaxies. We cross correlate the DR9 density field with the templates of imaging realities to assess the effectiveness of treatment methods and to characterize the significance of residual systematic error. Section 2 describes the DR9 sample and simulations with and without PNG and imaging systematic effects, and Section 3 outlines the theory for modeling angular power spectrum and analysis techniques for quantifying various observational systematic effects. Finally, we present the results in Section 4, and conclude with a comparison to previous f_{NL} constraints in Section 5.
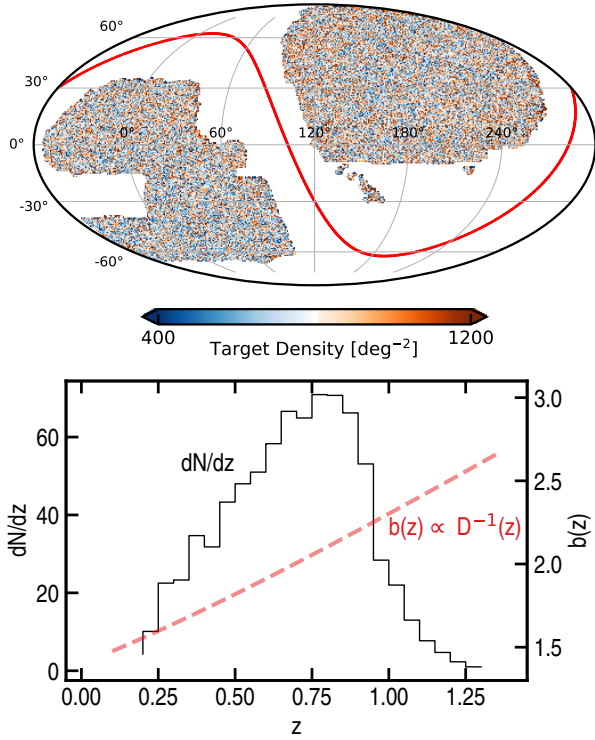
Figure 1. Top: Observed density field of DESI Luminous Red Galaxies Data Release 9 (Dey et al 2018) in deg^{-2} . Spurious disconnected islands from the DECaLS North footprint at Declination below −11 and parts of the DECaLS South with Declination below −30 are dropped from the DR9 sample due to potential calibration issues. Bottom: Redshift distribution and bias evolution of DESI LRGs (Zhou et al. 2021, 2022) (Zhou et al 2021, Zhou et al 2022, Dawson et al 2022). The redshift distribution is deducted from spectroscopy and the bias model assumes a constant clustering amplitude.

2 DATA

2.1 DR9 LRGs

Luminous red galaxies (LRGs) are massive galaxies that lack active star formation and considered as one of the highly biased tracers of large scale structure. Redshift of LRGs can be easily determined from a break around 4000 Å in their spectra. LRGs are widely targeted in previous galaxy redshift surveys (see, e.g., Eisenstein et al 2001, Prakash et al 2016), and their clustering and redshift properties are well studied (see, e.g., Reid et al 2016). DESI is expected to collect spectra of millions of LRGs covering the redshift range of $0.4 < z < 1.0$ over the span of its five year mission. Targets for DESI spectroscopy are selected from imaging surveys; The ground-based surveys that probe the sky in the optical bands are the Mayall z-band Legacy Survey using the Mayall telescope at Kitt Peak, USA (see e.g. Dey et al. 2018), the Beijing–Arizona Sky Survey using the Bok telescope at Kitt Peak (Zou et al. 2017), and the DECam Legacy Survey (DECaLS) using the Blanco telescop at Cerre-tololo, Chile. Additionally, the Legacy Surveys program takes advantage of another imaging survey, the Dark Energy Survey, for about $1130\,\mathrm{deg}^2$ of their southern sky footprint (Dark Energy Survey Collaboration; Fermilab & Flaugher 2005). The BASS+MzLS footprint can be distinguished from the DECaLS by applying DEC > 32.375 degrees, although there is an overlap between the two region for calibration.

We use photometric LRGs selected from the DESI Imaging Surveys Data Release 9 (DR9; Dey et al. 2018) using the selection

designed for the DESI 1% survey (Dawson et al 2022), described as SV3 in Zhou et al. (2022). The color-magnitude cuts are described in the g, r, z bands in the optical and $W1$ band in the infrared, and summarized here in Tab. 1. The implementation of these selections in the DESI pipeline is described in Myers et al (2022). DESI-like LRGs are selected brighter than the survey depth limits, and thus the sample density field is nearly homogenous. To further reduce stellar contamination, the sample is masked for bright stars, foreground bright galaxies as well as clusters of galaxies [1]. Then, it is binned into HEALPIX (Gorski et al. 2005) at NSIDE = 256 to construct the density map with an average density of 800 deg^{-2} with a coverage around 14, 000 square degrees of the sky. The density map is corrected for pixel incompleteness in the density field of LRGS using a catalog of random points, hereafter referred to as randoms, uniformly scattered over the footprint with the same cuts and masks applied to the DR9 LRGs.

Fig. 1 (top) shows observed density field of DR9 LRGs in deg^{-2} before accounting for any potential systematic effects. There are some disconnected islands, hereafter referred to as *spurious islands*, in the DECaLS North region at Declination below −11, which are removed from the sample to minimize potential calibration issues. Additionally, parts of the DECaLS South with Declination below −30 are cut from the sample, since similar calibration issues might tamper with our analysis. We present how these data cuts influence our f_{NL} constraints in Section 4. Fig. 1 (bottom) illustrates the redshift distribution of our sample which is inferred from the DESI Survey Validation data (Dawson et al 2022), and the evolution of galaxy bias for our LRG sample adapted from Zhou et al. (2021), consistent with the assumption of a constant clustering amplitude.

We study the impact of potential sources of systematic error, mapped into HEALPIX at the same NSIDE. Similar to Zhou et al. (2022), the properties studied in this work are local stellar density constructed from point-like sources with a g-band magnitude in the range $12 \le g < 17$ from Gaia Data Release 2 (see, Gaia Collaboration et al. 2018; Myers et al. 2022); Galactic extinction E[B-V] from Schlegel et al. (1998); and other imaging properties include survey depth (galaxy depth in the g, r, and z bands and PSF depth in W1) and seeing in the g, r, and z bands. These maps are produced by making the histograms of randoms (painted with imaging properties) in HEALPIx and averaging over randoms in each pixel. Fig. 3 shows the Pearson correlation between galaxy density and imaging properties in the top panel and the correlation among imaging properties themselves in the bottom panel. There is strong correlation between galaxy density and depth maps and then the second important property seems to be Galactic foregrounds. There is a little correlation between galaxy density and the W1 depth and psfsize properties. We find that there is a large correlation among the imaging properties themselves, especially the r-band and g-band properties are more correlated with each other than with the z-band. We derive a set of weights to account for spurious fluctuations by regressing out galaxy counts against a set of imaging maps. We consider both linear and nonlinear models. Parameters of the models are fit by optimizing the negative Poisson log likelihood, $= \lambda - y \log(\lambda)$, where ρ is the galaxy density and λ is the model defined as $\lambda = \log(1 + e^{f(u)})$ where u is either a linear function or a nonlinear function of imaging maps. For the linear model, we perform a Monte Carlo Markov Chain (MCMC) using the EMCEE package CITE and for the nonlinear model we use the

---

[1] See the maskbits at https://www.legacysurvey.org/dr9/bitmasks/

Table 1. Selection criteria for the DESI-like LRG targets from Zhou et al (2022).

Footprint	Criterion	Description
DECaLS	$z_{\text{fiber}} < 21.7$	Faint limit
	$z - W1 > 0.8 \times (r - z) - 0.6$	Stellar rejection
	$[(g - r > 1.3) \text{ AND } ((g - r) > -1.55 * (r - W1) + 3.13)] \text{ OR } (r - W1 > 1.8)$	Remove low-z galaxies
	$[(r - W1 > (W1 - 17.26) * 1.8) \text{ AND } (r - W1 > W1 - 16.36)] \text{ OR } (r - W1 > 3.29)$	Luminosity cut
BASS+MzLS	$z_{\text{fiber}} < 21.71$	Faint limit
	$z - W1 > 0.8 \times (r - z) - 0.6$	Stellar rejection
	$[(g - r > 1.34) \text{ AND } ((g - r) > -1.55 * (r - W1) + 3.23)] \text{ OR } (r - W1 > 1.8)$	Remove low-z galaxies
	$[(r - W1 > (W1 - 17.24) * 1.83) \text{ AND } (r - W1 > W1 - 16.33)] \text{ OR } (r - W1 > 3.39)$	Luminosity cut

implementation from Rezaie et al (2021). The nonlinear model is a neural network model with three hidden layers and 20 rectifier units on each layer. Rectifier is defined as $\max(0, u)$, and introduces the nonlinearity in the neural network. For the nonlinear approach we use 60% for training, 20% for validation, and 20% for testing. By changing the permutation of training-testing splits, we test the nonlinear model on entire data. The training is performed using ADAM optimize, which is a variant of gradient descent, and the learning rate is tuned on a validation set to dynamically varying between 0.001 and 0.1, to enable learning robust against local minima.

2.2 Lognormal Simulations

Lognormal distributions are shown to be appropriate for describing matter density fluctuations on large scales (Coles & Jones 1991). Unlike N-body simulations, the generation of lognormal density fields is rather quick and enables a computationaly cheap method to create a large number of realizations, validate analysis pipelines, and construct covariance matrices for error estimation. FLASK (Full-sky Lognormal Astro-fields Simulation Kit; Xavier et al. 2016) is used to generate two series of 1000 lognormal galaxy density fields with $f_{\text{NL}} = 0$ and 76.92 using $b(z) = 1.43/D(z)$. The fiducial cosmology to generate the mocks is based on a flat ΛCDM universe including one massive neutrino with $m_\nu = 0.06$ eV, and the rest of cosmological parameters are chosen within 68% of the Planck 2018 resutls (Planck 2018),

$$h = 0.67, \Omega_M = 0.31, \sigma_8 = 0.8, \text{ and } n_s = 0.97.$$

We use the same fiducial cosmology for the analysis of DR9 sample. These parameters are not degenerate with f_{NL}, however the impact of the fiducial cosmology on f_{NL} constraints is further investigated in Appendix ?.

3 METHODOLOGY

3.1 Measuring Power Spectrum

Galaxy density contrast in pixel i is defined as,

$$\hat{\delta}_i = \frac{\rho_i}{\hat{\bar{\rho}}} - 1, \tag{3}$$

where ρ is the density of galaxies accounted for pixel area $f_{\text{pix},i}$ and $\hat{\bar{\rho}}$ is the mean galaxy density estimated by,

$$\hat{\bar{\rho}} = \frac{\sum_i \rho_i f_{\text{pix},i}}{\sum_i f_{\text{pix},i}}. \tag{4}$$

By definition, Eqs. 3 and 4 ensure that the integral of the observed quantity over the footprint vanishes:

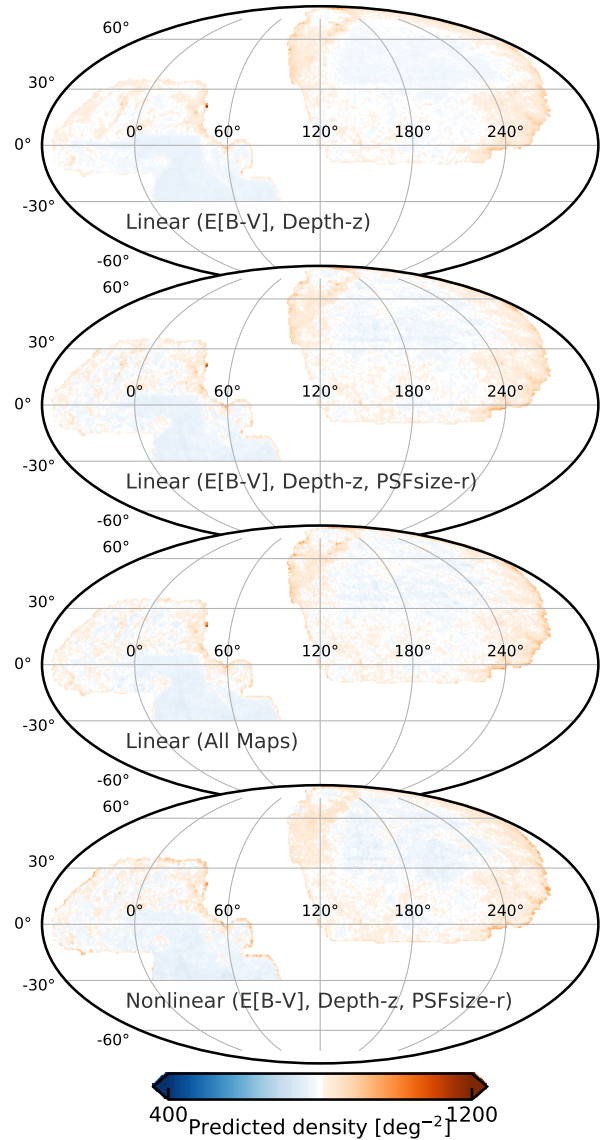$$\sum_i \hat{\delta}_i f_{\text{pix},i} = 0, \tag{5}$$

Figure 2. Predicted galaxy counts from template regression. Baseline approach uses imaging maps from Zhou et al. (2022): EBV, galaxy depth in rgz, psfdepth in W1, and psfsize in grz. Conservative I uses EBV and galaxy depth in z, and Conservative II uses EBV, galaxy depth in z, and psfsize in r. In all approaches, the models are regressed on BASS+MzLS, DECaLS North, and DECaLS South separately.
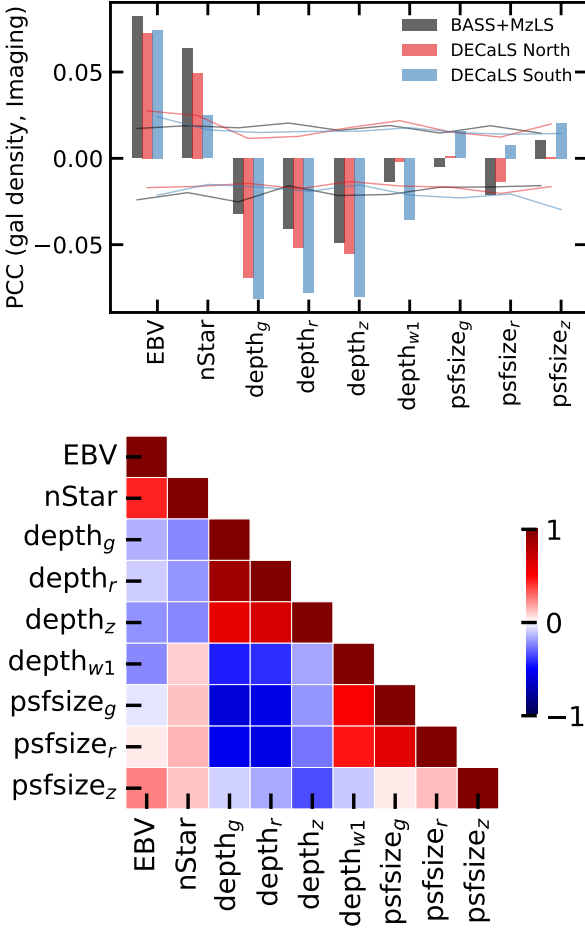
Figure 3. Top: Pearson-r correlation coefficient between galaxy density and imaging properties in the three imaging regions (top) and between imaging properties themselves for the full DESI footprint (bottom). Solid curves represent the range of correlations observed in 100 randomly selected mock realizations.

To estimate power spectrum, we expand the galaxy overdensity field in terms of Legendre polynomials,

$$\hat{\delta}_i = \sum_{\ell=0}^{\ell_{\max}} \sum_{m=-\ell}^{\ell} a_{\ell m} Y_{\ell m}(\theta_i, \phi_i), \qquad (6)$$

where θ, ϕ represent the polar and azimuthal angular coordinates of pixel i, respectively. The cutoff at $\ell = \ell_{\max}$ assumes that modes with $\ell > \ell_{\max}$ do not contribute significantly to signal power. The coefficients $a_{\ell m}$ are then obtained by integrating the density contrast field over the total number of non-empty pixels N_{pix} and using the orthogonality of Legendre polynomials:

$$\hat{a}_{\ell m} = \frac{4\pi}{N_{\mathrm{pix}}} \sum_{i=1}^{N_{\mathrm{pix}}} \hat{\delta}_i \, f_{\mathrm{pix},i} \, Y_{\ell m}^*(\theta_i, \phi_i), \qquad (7)$$

where * represents the complex conjugate. Then, the angular power spectrum estimator is defined as the variance of $\hat{a}_{\ell m}$ coefficients:

$$\hat{C}_\ell = \frac{1}{2\ell+1} \sum_{m=-\ell}^{\ell} \hat{a}_{\ell m} \hat{a}_{\ell m}^*. \qquad (8)$$

In order to extract $\hat{a}_{\ell m}$ and compute the angular power spectrum, C_ℓ, we make use of the ANAFAST function from HEALPix

(Gorski et al. 2005) with the third order iteration of the quadrature to increase the accuracy[2]. Due to the survey geometry implicit in the summation over the non-empty pixels and explicit in $f_{\mathrm{pix},i}$, our estimator does not return an unbiased estimate of power spectrum, and thus the same effect must be accounted in the modeling of power spectrum. Throughout this manuscript, we bin each mode with $\Delta\ell = 2$ between $\ell = 2$ and 20 and $\Delta\ell = 10$ from $\ell = 20$ to 300, while weighting each mode by $2\ell + 1$.

3.2 Modeling Power Spectrum

The projected angular power spectrum of galaxies in the presence of redshift space distortions and local primordial non-Gaussianity is related to the 3D linear power spectrum $P(k)$ and shotnoise N_{shot} by (see, e.g., Slosar et al. 2008),

$$C_\ell = \frac{2}{\pi} \int_0^\infty \frac{dk}{k} k^3 P(k) |\Delta_\ell(k)|^2 + N_{\mathrm{shot}}, \qquad (9)$$

where N_{shot} is the scale-independent shotnoise, and $\Delta_\ell(k) = \Delta_\ell^{\mathrm{g}}(k) + \Delta_\ell^{\mathrm{RSD}}(k) + \Delta_\ell^{\mathrm{f_{NL}}}(k)$ with,

$$\Delta_\ell^{\mathrm{g}}(k) = \int \frac{dr}{r} r b(r) D(r) \frac{dN}{dr} j_\ell(kr), \qquad (10)$$

$$\Delta_\ell^{\mathrm{RSD}}(k) = -\int \frac{dr}{r} r f(r) D(r) \frac{dN}{dr} j_\ell''(kr), \qquad (11)$$

$$\Delta_\ell^{\mathrm{f_{NL}}}(k) = f_{\mathrm{NL}} \frac{\alpha}{k^2 T(k)} \int \frac{dr}{r} r [b(r) - p] \frac{dN}{dr} j_\ell(kr), \qquad (12)$$

where $\alpha = 3\delta_c \Omega_M (H_0/c)^2$, $b(r)$ is the linear bias, dN/dr is the normalized redshift distribution of galaxies[3], δ_c is the critical density above which gravitational collapse occurs, $D(r)$ is the normalized growth factor such that $D(0) = 1$, $f(r)$ is the growth rate, and r is the comoving distance. The parameter p is the response of the tracer to halo's gravitational field, e.g., 1 for luminous red galaxies and 1.6 for recent mergers. In order to overcome rapid oscillations in spherical Bessel functions, we employ the FFTLog[4] algorithm and its extension as implemented in Fang et al (2020) to compute the inner integrations over $d \ln r$.

For a galaxy survey that observes the sky partially, the measured power spectrum is convolved with the survey geometry. This means that the pseudo-power spectrum $\hat{C}_\ell$ obtained by the direct Spherical Harmonic Transforms of a partial sky map, differs from the full-sky angular spectrum C_ℓ. However, their ensemble average is related by (**?**)

$$< \hat{C}_\ell > = \sum_{\ell'} M_{\ell\ell'} < C_{\ell'} >, \qquad (13)$$

where $M_{\ell\ell'}$ represents the mode-mode coupling from the partial sky coverage. This is known as the Window Function effect and a proper assessment of this effect is crucial for a robust measurement of the large-scale clustering of galaxies. This window effect is a source of observational systematic error and impacts the measured galaxy clustering, especially on scales comparable to survey size.

We follow a similar approach to that of (**?**) to model the window function effect on the theoretical power spectrum C_ℓ rather

---

[2] We refer the reader to https://healpix.sourceforge.io/pdf/subroutines.pdf, p. 104-105.
[3] $dN/dr = (dN/dz) * (dz/dr) \propto (dN/dz) * H(z)$
[4] github.com/xfangcosmo/FFTLog-and-beyond

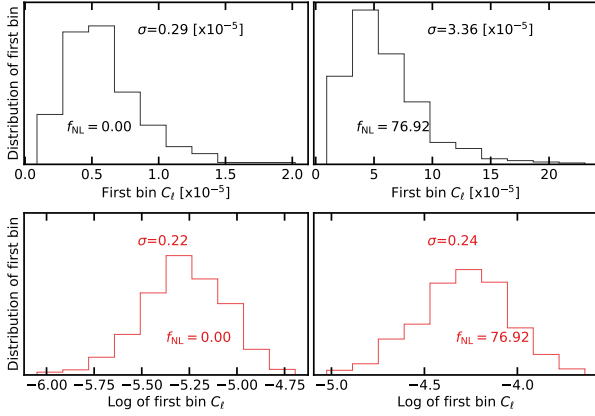**Figure 4.** Distribution of the first bin power spectrum for $f_{NL} = 0$ and 100 mocks.

than correcting the measured pseudo-power spectrum from data. First, we use HEALPIX to compute the pseudo-power spectrum of the window $\hat{C}_\ell^{\text{window}}$, which is defined by a mask file in ring ordering format with NSIDE= 256. Then, we transform it to correlation function by,

$$\omega^{\text{window}}(\theta) = \frac{1}{4\pi} \sum_\ell (2\ell + 1)\hat{C}_\ell^{\text{window}} P_\ell(\cos\theta). \tag{14}$$

Next, we normalize ω^{window} such that it is normalized to one at $\theta = 0$. Finally, we multiply the theory correlation function by ω^{window} and transform the result back to ℓ-space,

$$\hat{\omega}^{\text{model}} = \omega^{\text{model}}\omega^{\text{window}} \tag{15}$$

$$\hat{C}_\ell^{\text{model}} = 2\pi \int d\theta \hat{\omega}^{\text{model}}(\theta) P_\ell(\cos\theta). \tag{16}$$

The integral of the galaxy density contrast δ on the footprint is bound to zero, which is often referred to as the *Integral Constraint*. We account for this effect in the modeling by,

$$\hat{C}_\ell^{\text{model,IC}} = \hat{C}_\ell^{\text{model}} - \hat{C}_{\ell=0}^{\text{model}}\left(\frac{\hat{C}_\ell^{\text{window}}}{\hat{C}_{\ell=0}^{\text{window}}}\right) \tag{17}$$

3.3 Characterization of residual systematic error

We use the diagnostic tests presented in Rezaie et al 2021 based on cross power spectrum between galaxy density field and imaging maps and mean density contrast as a function of imaging properties to quantify the significance of imaging systematic effects.

3.3.1 Cross Spectrum

Taking $C_\ell^{g,x}$ as the cross power spectrum between galaxy density contrast field and imaging map, one can normalize this quantity by auto power spectrum of imaging map itself:

$$\hat{C}_{x,\ell} = \frac{(\hat{C}_\ell^{g,x})^2}{\hat{C}_\ell^{x,x}}, \tag{18}$$

and then construct a vector from cross spectra against all other imaging maps:

$$\hat{C}_{X,\ell} = [\hat{C}_{x_1,\ell}, \hat{C}_{x_2,\ell}, \hat{C}_{x_3,\ell}, ..., \hat{C}_{x_9,\ell}]. \tag{19}$$
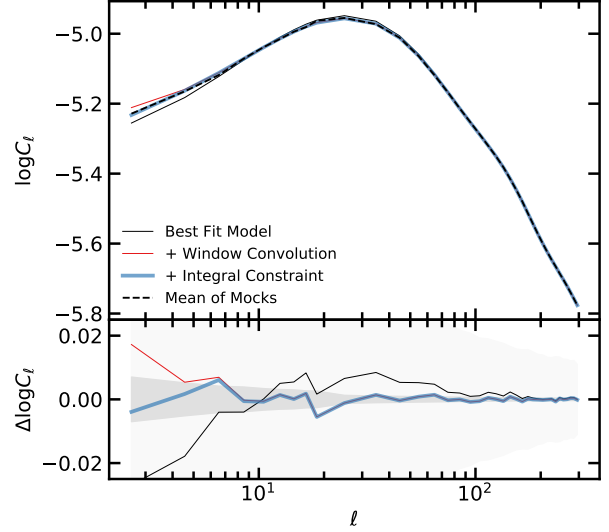

Figure 5. Mean power spectrum of 1000 mocks with $f_{NL} = 0$ and best fit theoretical prediction after accounting for various theoretical systematic effects.

We bin the C_X measurements with ℓ edges defined at 2, 10, 18, 26, 40, 60, 80, and 100. The mean and standard deviation of $\hat{C}_{X,\ell}$ for 1000 mocks with and without f_{NL} are shown in Fig. 6. Finally, cross power spectrum χ^2 can be defined as,

$$\chi^2 = C_{X,\ell}^T \mathbb{C}_X^{-1} C_{X,\ell}, \tag{20}$$

where covariance matrix $\mathbb{C}_X = < C_{X,\ell} C_{X,\ell'} >$ is constructed from mocks without systematic effects. This statistics is measured for every mock realization with the leave-one-out technique to construct a histogram, which is then compared to the χ^2 value observed from the DR9.

3.3.2 Mean Density

As an alternative test, we calculate the histogram of the density contrast field relative to each imaging map.

$$\delta_x = (\hat{\bar{\rho}})^{-1} \frac{\sum_i \rho_i f_{\text{pix},i}}{\sum_i f_{\text{pix},i}}, \tag{21}$$

where the summations are over pixels in each bin of imaging map x. Similarly, we construct the mean density contract vector against all imaging maps,

$$\delta_X = [\delta_{x_1}, \delta_{x_2}, \delta_{x_3}, ..., \delta_{x_9}], \tag{22}$$

and the total residual error as,

$$\chi^2 = \delta_X^T \mathbb{C}_\delta^{-1} \delta_X, \tag{23}$$

where the covariance matrix $\mathbb{C}_\delta = < \delta_X \delta_X >$ is constructed from mocks without systematic effects. Fig. 6 shows the cross power spectrum and mean density contrast for the DR9 LRG sample. The shades represent the 1σ level fluctuations observed in 1000 clean mocks with $f_{NL} = 0$ and 100.

3.4 Parameter estimation

We constrain f_{NL} by maximizing a posterior defined as,

$$-2\ln\mathcal{L} = (C(\Theta) - \hat{C})^\dagger \mathbb{C}^{-1}(C(\Theta) - \hat{C}) + \chi_{\text{priors}}^2, \tag{24}$$
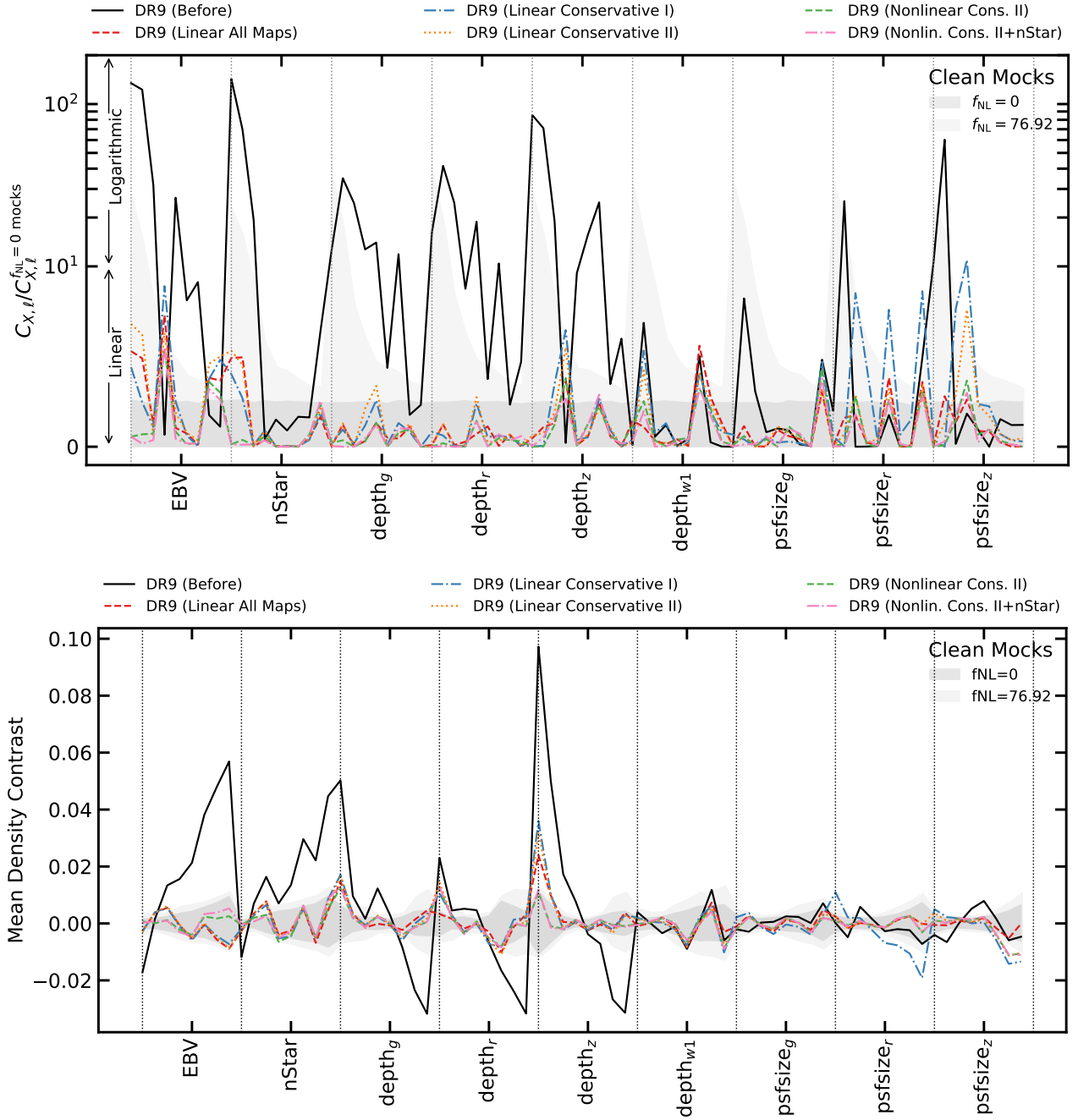
Figure 6. Residual systematic fluctuations of DR9 LRGs against imaging maps. Left: cross spectrum. Right: mean density contrast. Shades represent 1σ dispersion of 1000 clean mocks with and without $f_{\rm NL}$.

where Θ represents the parameters, $f_{\rm NL}$, bias at $z = 0$, and shotnoise, all of which were associated with a flat prior, $\chi^2_{\rm priors}$; $C(\Theta)$ is the (binned) theoretical power spectrum including the effects for survey geometry and integral constraint; $\hat{C}$ is the (binned) measured power spectrum; and $\mathbb{C}$ is the covariance matrix constructed from simulations.
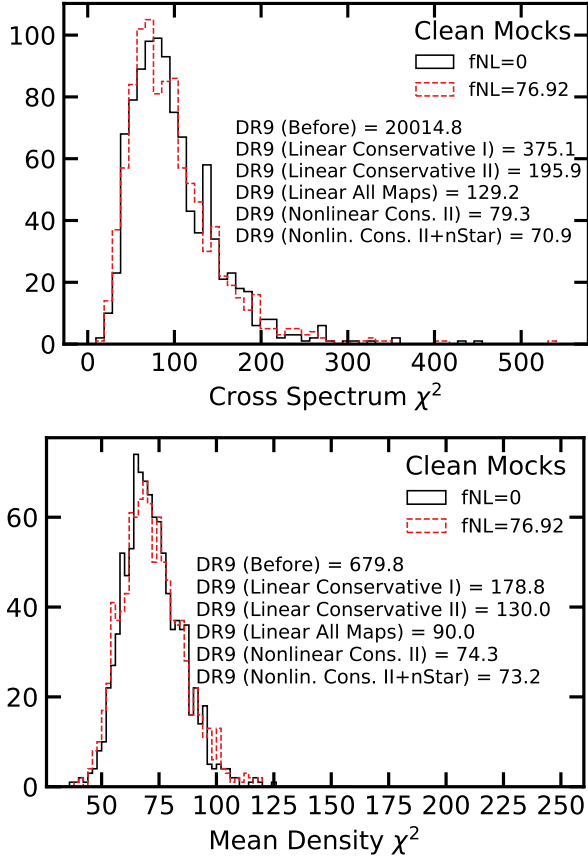
Figure 7. Left: Cross power spectrum χ^2 diagnostic. Right: Mean density contrast diagnostic. The values observed in DR9 before and after linear and nonlinear treatments are quoted and the histograms are constructed from 1000 realizations of clean mocks with $f_{\mathrm{NL}} = 0$ and 100.

4 RESULTS

TODO: The mean density and cross power spectrum χ^2 diagnostics do not reveal any signature of remaining systematic effects – given all the available templates. But we could be missing some unknown maps. There are some calibration maps made by Aaron which I need to look into. I did not use the Gaia stellar map for training– Zhou et al has a discussion on why it should not be used. But I plan to apply some cuts based on imaging (e.g., poor depth, high stellar density and extinction) to see if those impact the best fit estimates. Next, I will study how changing the lowest ell used could affect our results.

4.1 Lognormal Mocks

Corner plots of the PNG parameter f_{NL} and bias coefficient are shown in Fig. 8 for fitting the mean power spectrum of the mocks, with and without f_{NL}. Maximum-A-Posteriori estimates and marginalized mean, median and 1σ quantiles are summarized in Tab. 2. Comparing DECaLS North with sky coverage 0.14 to full DESI with 0.40, we find the constraint improve by a factor of 1.9 which is slightly more than $\sim f_{SKY}^{-1/2}$, 1.7. while As a robustness test, we also fit the mean power spectrum of the $f_{NL} = 100$ mocks using the covariance matrix estimated from the $f_{NL} = 0$ mocks. We find that the constraints improve by a factor of 4.2, due to a higher signal to noise ratio.

4.2 DR9 LRGs

4.3 Robustness Tests

4.3.1 Pixel completeness

We remove pixels with low completeness from the mask by applying $f_{pix} > 0.5$. At the cost of losing .6% survey area, we find that the f_{NL} constraint changes only around 2%, from 28.58 to 28.07, see *comp cut* Table 4.

4.3.2 Imaging quality

We remove pixels with poor imaging from the mask by applying the following limits on imaging properties; $E[B-V] < 0.1$, $nStar < 3000$, $depth_g > 23.2$, $depth_r > 22.6$, $depth_z > 22.5$, $psfsize_g < 2.5$, $psfsize_r < 2.5$, and $psfsize_z < 2$. We lose about 8.2% survey area, and the best fit f_{NL} estimate changes about 2% from 28.58 to 29.16. See *imag cut* in Table 4.

4.3.3 Covariance

The mocks with $f_{NL} = 76.92$ are used to construct a covariance matrix, and with the new covariance we obtain a 12% increase in the f_{NL} constraint uncertainties and 11% change in the best fit.

5 CONCLUSION

ACKNOWLEDGEMENTS

DATA AVAILABILITY

REFERENCES

Akrami Y., et al., 2019, arXiv preprint arXiv:1905.05697

Coles P., Jones B., 1991, Monthly Notices of the Royal Astronomical Society, 248, 1
Dalal N., Dore O., Huterer D., Shirokov A., 2008, Physical Review D, 77, 123514
Dey A., et al., 2018, arXiv preprint arXiv:1804.08657
Gaia Collaboration et al., 2018, A&A, 616, A1
Gorski K. M., Hivon E., Banday A. J., Wandelt B. D., Hansen F. K., Reinecke M., Bartelmann M., 2005, The Astrophysical Journal, 622, 759
Ho S., et al., 2015, J. Cosmology Astropart. Phys., 2015, 040
Komatsu E., Spergel D. N., 2001, Physical Review D, 63, 063002
Myers A. D., et al., 2022, arXiv e-prints, p. arXiv:2208.08518
Pullen A. R., Hirata C. M., 2013, Publications of the Astronomical Society of the Pacific, 125, 705
Schlegel D. J., Finkbeiner D. P., Davis M., 1998, The Astrophysical Journal, 500, 525
Schmittfull M., Seljak U., 2018, Phys. Rev. D, 97, 123540
Slosar A., Hirata C., Seljak U., Ho S., Padmanabhan N., 2008, Journal of Cosmology and Astroparticle Physics, 2008, 031
Weinberg D. H., Mortonson M. J., Eisenstein D. J., Hirata C., Riess A. G., Rozo E., 2013, Physics reports, 530, 87
Xavier H. S., Abdalla F. B., Joachimi B., 2016, Monthly Notices of the Royal Astronomical Society, 459, 3693
Zhou R., et al., 2021, Monthly Notices of the Royal Astronomical Society, 501, 3309
Zhou R., et al., 2022, arXiv preprint arXiv:2208.08515

Table 2. Maximum-A-Posteriori (MAP) and marginalized mean estimates for f_{NL} from fitting the mean power spectrum of the mocks. Degree of freedom is 34 (37 data points - 3 parameters).

|			f_{NL}				
True f_{NL}	Footprint	Observable	Best fit	Mean	68% CL	95% CL	χ^2
76.92	DESI	$\log C_\ell$	77.67	77.67	$77.17 < f_{NL} < 78.16$	$76.71 < f_{NL} < 78.64$	38.8
76.92	DESI	C_ℓ	77.67	77.65	$77.17 < f_{NL} < 78.14$	$76.70 < f_{NL} < 78.60$	39.0
76.92	DESI	$\log C_\ell + f_{NL} = 0$ cov	77.70	77.71	$77.25 < f_{NL} < 78.17$	$76.81 < f_{NL} < 78.63$	39.9
76.92	DESI	$C_\ell + f_{NL} = 0$ cov	77.03	77.02	$76.93 < f_{NL} < 77.12$	$76.83 < f_{NL} < 77.22$	207.6
0	DESI	$\log C_\ell$	0.36	0.36	$0.06 < f_{NL} < 0.65$	$-0.23 < f_{NL} < 0.94$	35.7
0	DECaLS North	$\log C_\ell$	0.07	0.06	$-0.47 < f_{NL} < 0.60$	$-1.00 < f_{NL} < 1.12$	26.7
0	DECaLS South	$\log C_\ell$	0.67	0.67	$0.13 < f_{NL} < 1.22$	$-0.40 < f_{NL} < 1.75$	34.3
0	BASS+MzLS	$\log C_\ell$	0.83	0.82	$0.25 < f_{NL} < 1.40$	$-0.31 < f_{NL} < 1.96$	39.4
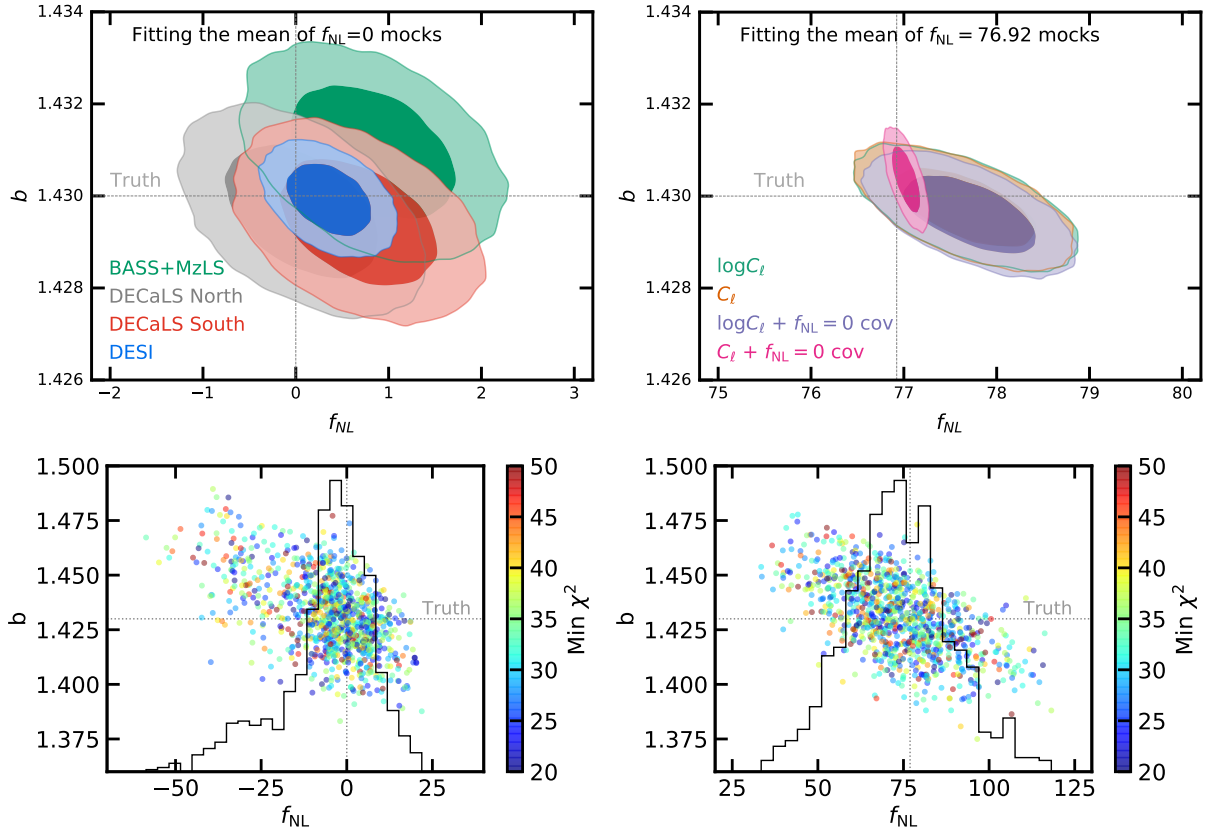
Figure 8. Top: 68% and 95% confidence contours for $f_{NL} = 0$ (left) and 100 (right) mocks. Using the $\log C_\ell$ fitting yield constraints that are insensitive to the covariance used. Bottom: best fit estimates from fitting 1000 lognormal mocks with $f_{NL} = 0$ (left) and 76.92 (right) in the DESI footprint. The truth values are represented by vertical and horizontal lines.

Table 3. Best fit and marginalized estimates for f_{NL} from fitting the mean power spectrum of the mocks before and after applying imaging weights.

Mock	Method	f_{NL} Best fit	Mean	68% CL	95% CL	χ^2
0	No Weight	0.36	0.36	$0.06 < f_{NL} < 0.65$	$-0.23 < f_{NL} < 0.94$	35.7
0	ConsII	-11.64	-11.65	$-12.00 < f_{NL} < -11.30$	$-12.34 < f_{NL} < -10.97$	86.8
0	ConsII+nStar	-20.14	-20.13	$-20.44 < f_{NL} < -19.82$	$-20.74 < f_{NL} < -19.52$	472.8
0	All Maps+nStar	-26.91	-26.92	$-27.16 < f_{NL} < -26.68$	$-27.39 < f_{NL} < -26.46$	5481.0
Contaminated 0	ConsII	-12.12	-12.13	$-12.48 < f_{NL} < -11.78$	$-12.83 < f_{NL} < -11.44$	94.0
Contaminated 0	ConsII+nStar	-20.97	-20.98	$-21.28 < f_{NL} < -20.67$	$-21.58 < f_{NL} < -20.37$	556.3
Contaminated 0	All Maps+nStar	-28.13	-28.13	$-28.36 < f_{NL} < -27.90$	$-28.59 < f_{NL} < -27.67$	6760.5
76.92	No Weight	77.67	77.67	$77.17 < f_{NL} < 78.16$	$76.71 < f_{NL} < 78.64$	38.8
76.92	ConsII	54.57	54.57	$54.14 < f_{NL} < 55.01$	$53.72 < f_{NL} < 55.45$	603.5
76.92	ConsII+nStar	38.38	38.38	$37.99 < f_{NL} < 38.78$	$37.60 < f_{NL} < 39.16$	537.0
76.92	All Maps+nStar	6.04	6.04	$5.72 < f_{NL} < 6.36$	$5.41 < f_{NL} < 6.67$	694.0
Contaminated 76.92	ConsII	54.01	54.00	$53.57 < f_{NL} < 54.44$	$53.15 < f_{NL} < 54.86$	588.0
Contaminated 76.92	ConsII+nStar	37.48	37.49	$37.09 < f_{NL} < 37.88$	$36.70 < f_{NL} < 38.27$	510.7
Contaminated 76.92	All Maps+nStar	4.59	4.58	$4.26 < f_{NL} < 4.90$	$3.95 < f_{NL} < 5.22$	649.7

Table 4. Maximum-A-Posteriori (MAP) and marginalized mean estimates for f_{NL} from fitting power spectrum of DR9 LRGs before and after correcting for systematics. Degree of freedom is 34 (37 data points - 3 parameters).

| Footprint	Method	f_{NL} Best fit	Mean	68% CL	95% CL	χ^2
DESI	No Weight	113.18	115.49	$98.14 < f_{NL} < 132.89$	$83.51 < f_{NL} < 151.59$	44.4
DESI	Linear (All Maps)	36.05	37.72	$26.13 < f_{NL} < 49.21$	$16.31 < f_{NL} < 62.31$	41.1
DESI	Linear (Conservative I)	49.58	51.30	$38.21 < f_{NL} < 64.33$	$27.41 < f_{NL} < 78.91$	38.8
DESI	Linear (Conservative II)	36.63	38.11	$26.32 < f_{NL} < 49.86$	$16.36 < f_{NL} < 63.12$	39.6
DESI	Nonlinear (Cons. II)	28.58	29.79	$18.91 < f_{NL} < 40.59$	$9.47 < f_{NL} < 52.73$	34.6
DESI	Nonlin. (Cons. II+nStar)	16.63	17.52	$7.51 < f_{NL} < 27.53$	$-1.59 < f_{NL} < 38.49$	35.2
DESI	Nonlin. (All Maps+nStar)	-5.87	-9.19	$-21.45 < f_{NL} < 2.40$	$-33.81 < f_{NL} < 12.06$	39.5
DESI (imag. cut)	Nonlin. (Cons. II)	29.16	30.57	$19.05 < f_{NL} < 42.18$	$9.01 < f_{NL} < 54.81$	35.8
DESI (comp. cut)	Nonlin. (Cons. II)	28.07	29.48	$18.38 < f_{NL} < 40.50$	$8.81 < f_{NL} < 53.10$	34.5
DESI	Nonlin. (Cons. II)+f_{NL} = 76.92 Cov	31.62	33.11	$20.94 < f_{NL} < 45.24$	$10.56 < f_{NL} < 59.16$	33.5
BASS+MzLS	Nonlin. (Cons. II)	15.43	19.01	$-1.17 < f_{NL} < 39.43$	$-19.19 < f_{NL} < 63.56$	35.6
BASS+MzLS	Nonlin. (Cons. II+nStar)	13.12	15.39	$-4.59 < f_{NL} < 35.56$	$-24.88 < f_{NL} < 59.31$	34.7
BASS+MzLS	Nonlin. (All Maps+nStar)	-3.73	-6.34	$-27.11 < f_{NL} < 13.75$	$-47.44 < f_{NL} < 33.94$	36.8
BASS+MzLS (imag. cut)	Nonlin. (Cons. II)	25.03	29.12	$6.16 < f_{NL} < 52.44$	$-14.22 < f_{NL} < 80.54$	36.2
BASS+MzLS (comp. cut)	Nonlin. (Cons. II)	16.99	20.90	$0.26 < f_{NL} < 41.76$	$-18.30 < f_{NL} < 67.12$	35.8
DECaLS North	Nonlin. (Cons. II)	41.02	44.89	$23.33 < f_{NL} < 66.78$	$4.96 < f_{NL} < 93.02$	41.1
DECaLS North	Nonlin. (Cons. II+CALIBZ+HI)	55.46	60.44	$36.78 < f_{NL} < 84.05$	$17.86 < f_{NL} < 112.81$	38.4
DECaLS North	Nonlin. (Cons. II+nStar)	31.45	34.78	$14.14 < f_{NL} < 55.79$	$-5.81 < f_{NL} < 80.80$	41.2
DECaLS North	Nonlin. (All Maps+nStar)	0.81	-5.68	$-29.73 < f_{NL} < 16.71$	$-53.15 < f_{NL} < 36.19$	45.1
DECaLS North + islands	Nonlin. (Cons. II)	41.05	44.82	$23.58 < f_{NL} < 66.08$	$6.40 < f_{NL} < 91.42$	40.7
DECaLS North (imag. cut)	Nonlin. (Cons. II)	43.27	48.39	$24.60 < f_{NL} < 72.50$	$4.71 < f_{NL} < 101.42$	35.1
DECaLS North (comp. cut)	Nonlin. (Cons. II)	40.55	44.63	$22.41 < f_{NL} < 67.11$	$3.95 < f_{NL} < 94.06$	41.4
DECaLS South	Nonlin. (Cons. II)	31.24	33.21	$14.89 < f_{NL} < 52.40$	$-5.11 < f_{NL} < 74.35$	30.2
DECaLS South	Nonlin. (Cons. II+CALIBZ+HI)	33.79	37.50	$17.71 < f_{NL} < 57.42$	$-0.31 < f_{NL} < 80.94$	30.8
DECaLS South	Nonlin. (Cons. II+nStar)	14.34	6.28	$-21.19 < f_{NL} < 30.01$	$-53.63 < f_{NL} < 49.51$	31.9
DECaLS South	Nonlin. (All Maps+nStar)	-36.76	-32.01	$-49.38 < f_{NL} < -13.61$	$-65.26 < f_{NL} < 7.52$	31.5
DECaLS South + DEC < -30	Nonlin. (Cons. II)	43.79	46.79	$30.16 < f_{NL} < 63.41$	$16.38 < f_{NL} < 82.72$	23.8
DECaLS South (imag. cut)	Nonlin. (Cons. II)	26.47	23.36	$3.18 < f_{NL} < 47.84$	$-57.69 < f_{NL} < 71.39$	30.0
DECaLS South (comp. cut)	Nonlin. (Cons. II)	29.62	31.76	$13.00 < f_{NL} < 51.58$	$-9.78 < f_{NL} < 74.28$	29.7
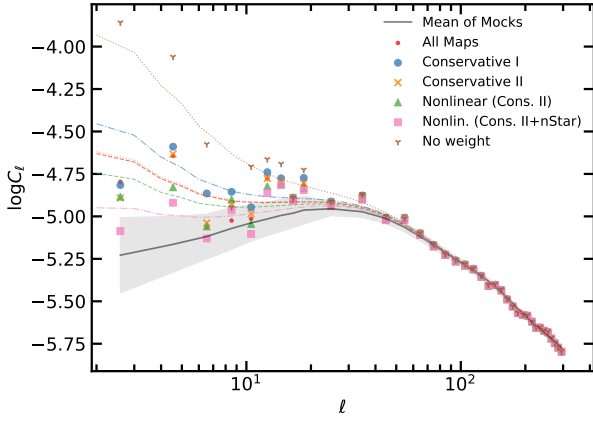
Figure 9. Measured power spectrum of the DR9 LRG sample before and after correcting for systematics with their corresponding best fit theory predictions. The shade represents 1σ error constructed from the $f_{\rm NL} = 0$ mocks.
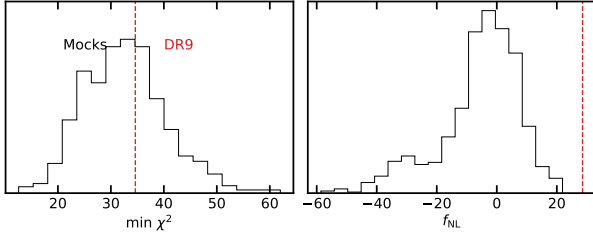

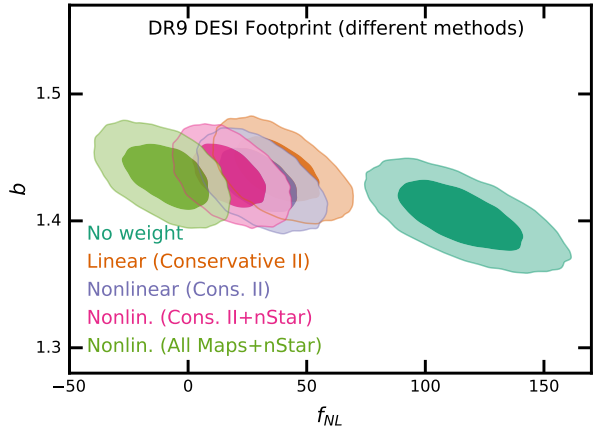**Figure 10.** Best fit χ^2 and $f_{\rm NL}$ from fitting mocks (histograms) and DR9 (vertical line).

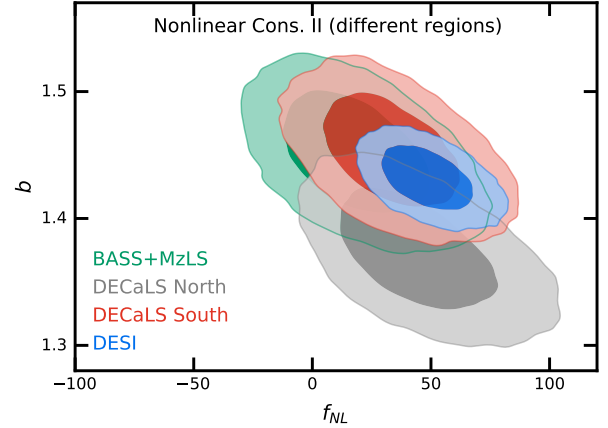**Figure 11.** DR9 constraints. DESI footprint before and after applying various cleaning methods.

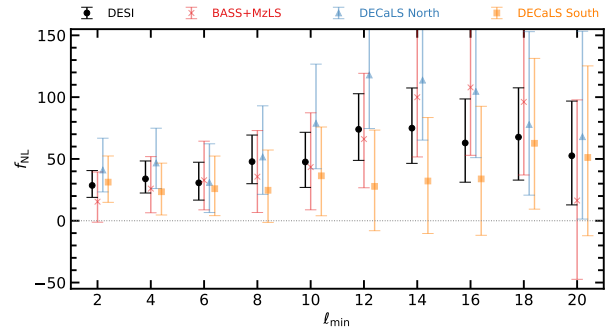**Figure 12.** DR9 constraints. Each individual imaging survey versus the whole DESI footprint.

Figure 13. DR9 Constraints. Mean estimates of $f_{\rm NL}$ and its 65% and 95% errorbars after changing the lowest ℓ mode used in fitting.
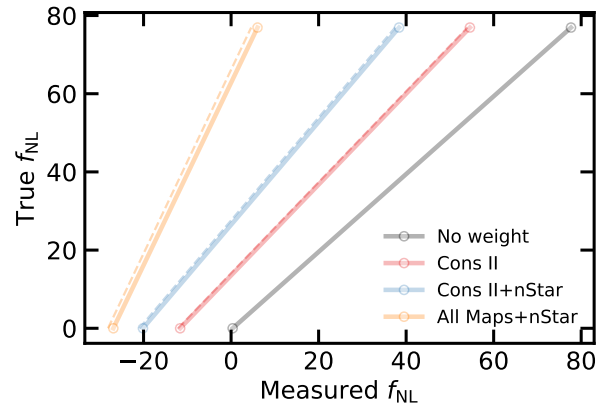

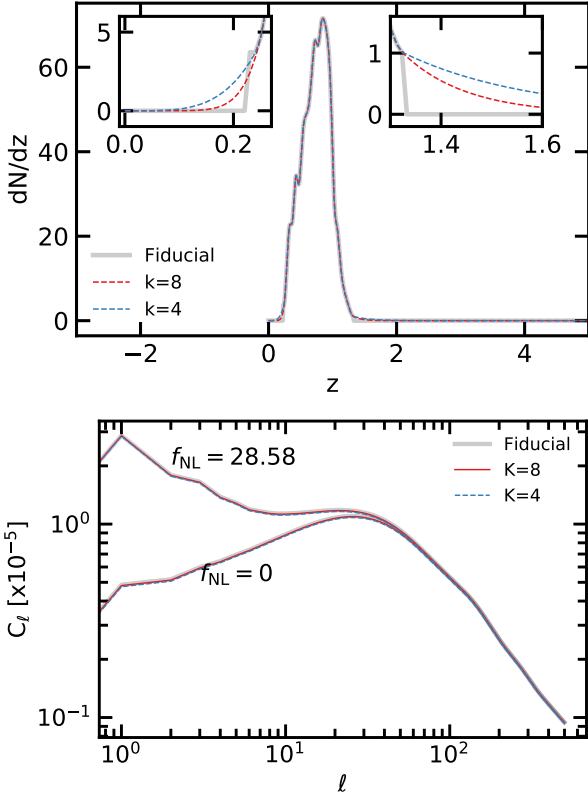**Figure 14.** True $f_{\rm NL}$ vs measured $f_{\rm NL}$ from mocks with (dashed) and without systematics (solid).

Figure A1. Top: Redshift distribution of LRGs. Bottom: Power spectrum given various dN/dz treatments for two arbitrary f_{NL} values.

Figure B1. Cross Spectrum χ^2 as a function of the highest mode ℓ_{max}. The lowest mode is $\ell_{min} = 2$.

APPENDIX A: REDSHIFT DISTRIBUTION

Redshift distribution of LRGs is constructed from the DESI SV data release of Denali with the same selection. The fiducial distribution only covers the redshift range from 0.2 to 1.35. Below we test the impact of LRG dN/dz on the angular power spectrum.

APPENDIX B: SCALE DEPENDENCE SYSTEMATICS

The default modes used in calculating the cross spectrum χ^2 diagnostic range for $2 \leq \ell < 20$. Here we further test the stability of our results by extending the highest mode out to $\ell = 100$ or fluctuations over scales as small as 1.8 degrees.
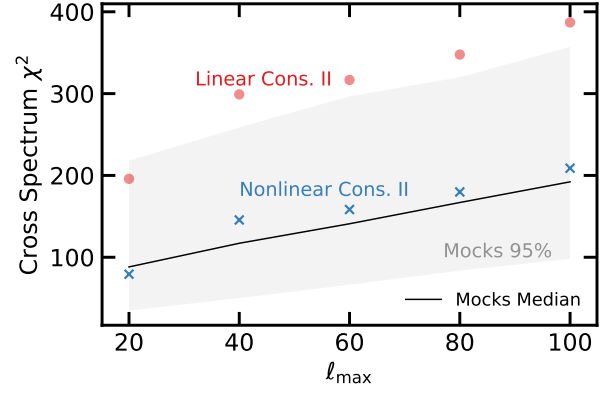
This paper has been typeset from a TEX/LATEX file prepared by the author.